JACS Au
AN OPEN ACCESS JOURNAL OF THE AMERICAN CHEMICAL SOCIETY

Editors' Choice
Open Access

pubs.acs.org/jacsau
Article

Unveiling Hidden Shake-Up Features in the Uranyl M_4-Edge Spectrum

Jordan N. Ehrman,[‖] Kirill Shumilov,[‖] Andrew J. Jenkins,[‖] Joseph M. Kasper, Tonya Vitova, Enrique R. Batista, Ping Yang,* and Xiaosong Li*

Cite This: *JACS Au* 2024, 4, 1134−1141

Read Online

ACCESS | Metrics & More | Article Recommendations | Supporting Information

ABSTRACT: The $M_{4,5}$-edge high energy resolution X-ray absorption near-edge structure (HR-XANES) spectra of actinyls offer valuable insights into the electronic structure and bonding properties of heavy-element complexes. To conduct a comprehensive spectral analysis, it is essential to employ computational methods that accurately account for relativistic effects and electron correlation. In this work, we utilize variational relativistic multireference configurational interaction methods to compute and analyze the X-ray M_4-edge absorption spectrum of uranyl. By employing these advanced computational techniques, we achieve excellent agreement between the calculated spectral features and experimental observations. Moreover, the calculations unveil significant shake-up features, which arise from the intricate interplay between strongly correlated 3d core-electron and ligand excitations. This research provides important theoretical insights into the spectral characteristics of heavy-element complexes. Furthermore, it establishes the foundation for utilizing $M_{4,5}$-edge spectroscopy as a means to investigate the chemical activities of such complexes. By leveraging this technique, we can gain a deeper understanding of the bonding behavior and reactivity of heavy-element compounds.

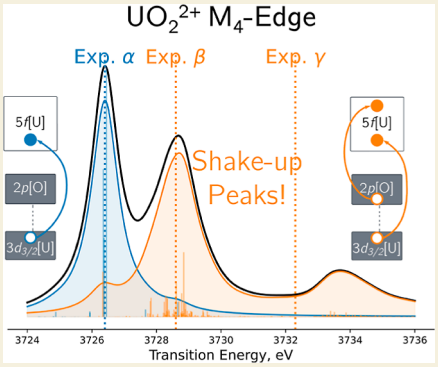

KEYWORDS: *heavy element, M-edge spectroscopy, core electron excitation, X-ray absorption, shake-up peaks*

The chemistry of actinide complexes is foundational to a variety of applications, including not only nuclear waste separations[1,2] but also catalysis[3,4] and nanomaterials.[5−7] However, the electronic structure and bonding of heavy elements remain less well-understood than metal−ligand bonding with light elements, with the covalency of the 5f electrons playing a central role.[8,9] X-ray spectroscopy has become an experimental tool of choice as the characteristics of the X-ray spectrum are not only element-specific but also sensitive to the chemical environment. Analyses of the spectral shifts and intensities at the M-edge (excitations from the $n = 3$ orbital level) have been shown to provide important information about the covalency of 5f electrons in the bonding interactions of heavy elements.[10−17] M-edge absorption spectra calculations, similar to that of L-edge spectra,[18,19] necessitate the use of a relativistic treatment, including scalar relativistic and spin−orbit coupling terms. The complexity of the electronic structures of heavy elements poses a challenging frontier in the theoretical prediction of their M-edge spectra due to the need to treat relativistic effects (scalar relativities and spin−orbit couplings) as well as static and dynamic correlations on an equal footing.

Recent advances in variational relativistic many-body theory[20−24] have opened a new avenue to provide accurate calculations that can complement and interpret new multifaceted experimental probes of heavy-element complexes. In the framework of a variational relativistic multireference configuration interaction (MRCI) approach,[22,25] relativistic corrections are included in the orbital optimization, and the static correlation is described by the complete active space self-consistent-field (CASSCF), followed by an additional configuration interaction (CI) treatment to add dynamic correlation. In this work, we investigate the spectroscopic features of the uranyl ion (UO_2^{2+}) M-edge spectrum using the variational relativistic exact-two-component (X2C) MRCI approach (see the Methods section), aiming to provide a very accurate probe into the spectral characteristics of early actinide complexes. Fundamental knowledge gleaned from this study will aid in our understanding of the electronic structures of uranium complexes. These complexes can exhibit unique reactivities and photophysical properties, underpinning their vital role in various areas of chemical science.[26]

Figure 1 illustrates the molecular orbital (MO) diagram for uranyl, providing a foundation for analyzing its electronic structure.[8,27,28] In $M_{4,5}$-edge XAS (X-ray absorption spectros-

Received: December 28, 2023
Revised: February 14, 2024
Accepted: February 15, 2024
Published: March 6, 2024

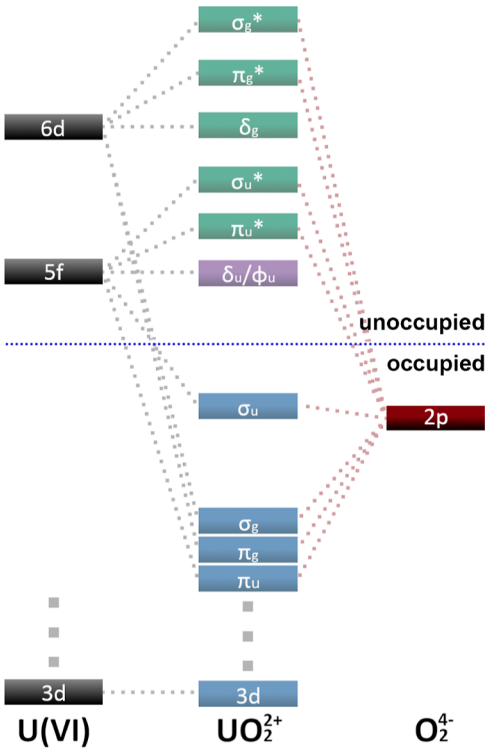

Figure 1. Uranyl qualitative molecular orbital diagram.

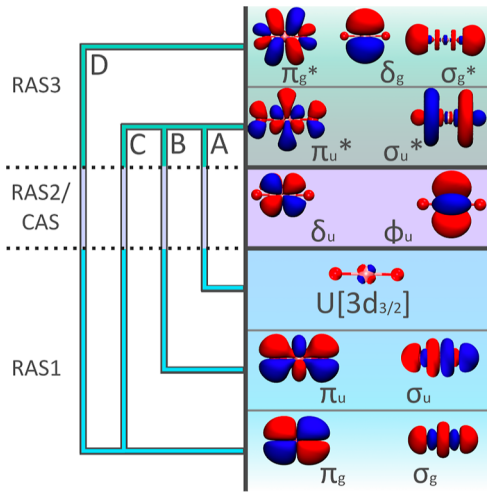

Figure 2. Uranyl X2C-MRCI partitioning schemes. **Schemes A**, **B**, **C**, and **D** progressively include a greater number of correlating orbitals and electrons, as detailed in the text regarding partitioning.

copy), the excitations from the uranium 3d orbitals to unoccupied frontier orbitals, including the 5f manifold, are probed following the $\Delta J = 0, \pm 1$ and $\Delta l = \pm 1$ selection rules. The lower-lying unoccupied orbitals consist of the nonbonding δ_u and ϕ_u type formed from the U[$5f_{z(x^2-y^2)}$], U[$5f_{xyz}$], U[$5f_{y(3x^2-y^2)}$], and U[$5f_{x(x^2-3y^2)}$] manifold. Through the mixing of U[5f] with the O[2p] orbitals, hybridized or covalent bonding is formed, leading to the occupied two π_u orbitals (hybridization of U[$5f_{yz^2}$] and U[$5f_{xz^2}$] with O[2p]) and a σ_u orbital (hybridization of U[$5f_{z^3}$] with O[2p]), all with the ungerade (u) symmetry. The hybridization of the U[6d] orbitals with O[2p] yield the bonding orbitals of gerade (g) symmetry, two π_g hybridizing uranium $6d_{xz}$ and $6d_{yz}$ and one σ_g hybridizing uranium $6d_{z^2}$. The antibonding counterparts reside in the unoccupied space, two π_u^*, two π_g^*, one σ_u^*, and one σ_g^*.

Previous works have shown that modeling X-ray spectra using time-dependent density functional theory (TDDFT) with relativistic corrections is capable of capturing some of the spectral features in uranyl core-excitations and yields qualitatively correct spectra.[29−31] However, the correlation captured by TDDFT is incomplete, shown by the importance of double excitations in the accurate modeling of M-edge spectra in multireference methods with perturbative spin−orbit coupling.[11,12,32] On the other hand, the manifestation of double excitation and its physical characteristics in the uranyl M-edge spectrum remain largely unexplored.

To investigate the intricate interplay between the 5f and 6d manifolds and to assess the impact of electron correlations observed in the uranyl M_4-edge HR-XANES, a comprehensive approach is employed. In this method, fully optimized core-hole orbitals including spin−orbit coupling are assigned to X2C-MRCI spaces, considering the RAS (restricted active space) partitioning scheme depicted in Figure 2 (for detailed computational information, please refer to the Methods section). Four distinct correlated X2C-MRCI schemes were carefully selected and designed to analyze the correlation effects arising from the bonding and antibonding 5f and 6d manifolds. These schemes systematically increase the size of the active space, allowing for a thorough investigation of the correlation effects in the system.

- **Scheme A** is considered the minimal X2C-MRCI scheme where RAS1 includes the four U[$3d_{3/2}$] core electrons and spinor orbitals (4 electrons and 4 orbitals) corresponding to the M_4-edge, and RAS3 includes four π_u^* and two σ_u^* antibonding U[5f]−O[2p] spinor orbitals (0 electron and 6 orbitals).
- **Scheme B** adds to **Scheme A** four π_u and two σ_u correlating electrons and spinor orbitals in RAS1 (10 electrons and 10 orbitals). RAS3 is the same as in **Scheme A**.
- **Scheme C** adds to **Scheme B** the four π_g and two σ_g correlating electrons and spinor orbitals, arising from U[6d]−O[2p] interactions, in RAS1 (16 electrons and 16 orbitals). RAS3 is the same as in **Scheme A**.
- **Scheme D** expands upon **Scheme C** by adding the four δ_g^*, four π_g^*, and two σ_g^* spinor orbitals in RAS3 (0 electron and 16 orbitals).

All schemes include the eight δ/ϕ orbitals in RAS2. These four X2C-MRCI schemes provide a valuable framework for assessing the significance of bonding orbitals in the 5f and 6d manifolds as well as the electron correlation contributions from antibonding orbitals, with respect to the spectral characteristics. It is worth noting that all schemes include the 3d core electrons of uranium, ensuring that excitations from the RAS1 space are responsible for the observed M_4-edge spectral features.

In these schemes, the RAS1 space allows for the inclusion of two core holes, while the RAS3 space permits the inclusion of two electrons. This restriction facilitates both single and double excitations from the RAS1 space. Consequently, this X2C-MRCI approach not only enables the calculation of single excitations but also facilitates the exploration of shake-up/shake-down or satellite states, offering a comprehensive understanding of the system's electronic structure.

https://doi.org/10.1021/jacsau.3c00838
JACS Au 2024, 4, 1134−1141

Figure 3 illustrates the computed uranyl M_4-edge spectra obtained using four distinct X2C-MRCI schemes, each

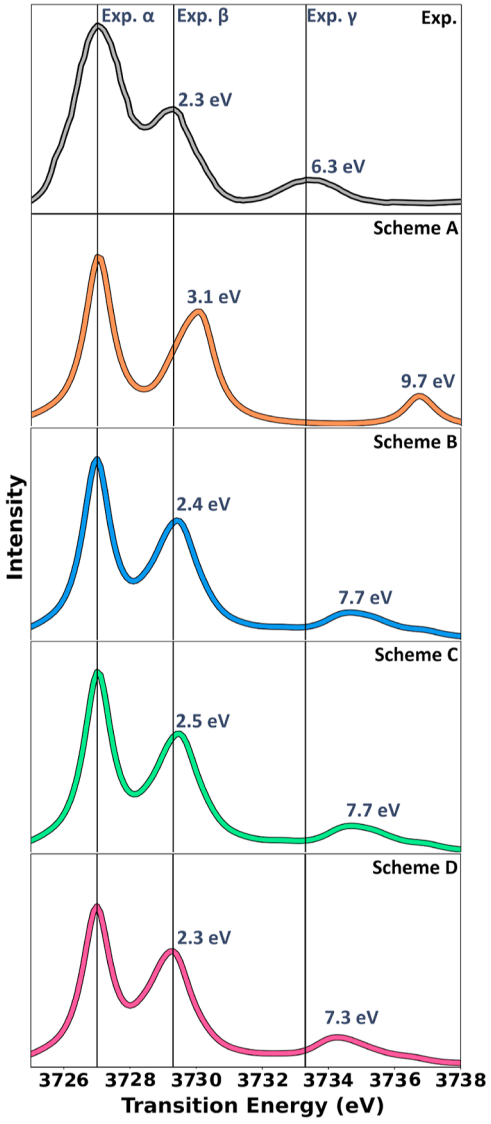

Figure 3. Uranyl M_4-edge calculated with X2C-MRCI using the four different active space schemes and an X2C-RASSCF core-hole reference, compared to experiment. Normalized intensities and excitation energies are shifted to be equal at the major peak. Lorentzian broadening parameter is set to an fwhm of 1.0 eV based on the observed experimental broadening profile. The calculated spectra under Schemes A, B, C, and D are shifted by 161.46, 158.32, 158.08, and 156.72 eV, respectively, to best align with the experimental α feature.

characterized by an increasing size of the correlation space, as previously described. Within the experimental spectral region, all calculations exhibit three prominent peaks denoted as α, β, and γ.

If no correlation of the inner valence bonding electrons is included—X2C-MRCI employing Scheme A—a qualitative agreement with the experiment is obtained, with spectral shifts of 3.1 and 9.7 eV for the β and γ peaks, respectively. However, a substantial improvement is achieved by incorporating correlating occupied π_u and σ_u orbitals through Scheme B, resulting in shifts of 2.4 and 7.7 eV for the β and γ peaks, respectively. The enhancement in predictive accuracy can be attributed to the consideration of electron correlations from covalent pairs of orbitals, π_u/σ_u and π_u^*/σ_u^*. This observation aligns with the expectation that these orbitals, involved in covalent bonding, play a crucial role in accurately describing the spectral behavior.

The accuracy of the spectral prediction improved with the inclusion of the 6d orbitals in the active space. In X2C-MRCI Scheme C, correlation with the 6d bonding orbitals (π_g and σ_g) is introduced, while Scheme D incorporates additional correlation involving the antibonding π_g^* and σ_g^* orbitals, as well as nonbonding δ_g orbitals. By expanding the correlation spaces with these additional orbitals, the convergence of the β peak in the uranyl M_4-edge spectrum toward the experimental result is achieved. Moreover, the inclusion of these orbitals through Scheme D results in a substantial improvement in the prediction of the γ peak, bringing it very close to the experimental observation.

Overall, we found that Scheme B successfully reached a converged result for the β peak and significantly improved the position of the γ peak, confirming previous theoretical investigations.[11,16,32] This observation suggests that including the correlating 5f bonding orbitals is crucial for the accurate prediction of the M-edge spectra of UO_2^{2+}.

The excellent agreement observed between the computed spectrum using X2C-MRCI and the experimental data instills a high level of confidence in the theoretical analysis of the spectral characteristics. To further deepen our understanding of the M_4-edge spectra, Figure 4 presents a partial intensity analysis that elucidates the contributions from specific MOs. This insightful analysis facilitates an enhanced comprehension of the underlying nature and distinctive features exhibited by the M-edge spectra.

In order of increasing energy, the three peaks were initially assigned to 3d → δ_u/ϕ_u, 3d → π_u^*, and 3d → σ_u^* transitions.[33] Such an assignment suggests that these transitions are nonoverlapping one-electron excitations. Given that the 3d → δ_u/ϕ_u transition is pinned in the spectrum, the splitting observed between the M_4-edge spectral peaks provides valuable insights into the level of covalency present, reflecting a similar concept to that of MO interaction.[10]

The spectral analysis conducted using Scheme A in Figure 4 confirms the initial experimental assignment, indicating simple single-electron excitations from $3d_{3/2}$ to δ_u/ϕ_u, π_u^*, and σ_u^* orbitals, respectively. While this agreement with the experimental peak positions and transition assignments seems reasonable, it is important to note that Scheme A lacks correlations arising from the 5f and 6d bonding orbitals. Without considering the correlations stemming from the 5f and 6d manifolds, the computed spectra may fail to capture the intricate electronic interactions and multielectron effects that can significantly influence the observed spectral features. Therefore, although Scheme A yields satisfactory agreement in terms of peak positions and transition assignments, it is crucial to recognize the potential limitations and the possibility of misinterpretation due to the absence of relevant correlations.

Indeed, the analysis of the partial intensity using the larger correlation spaces shows a very different picture and would suggest an alternative assignment of the transitions. The α peak predominantly involves transitions from the $3d_{3/2}$ manifold to the δ_u/ϕ_u nonbonding orbitals, aligning with our expectations. However, intriguingly, the presence of significant contributions from the nonbonding δ_u/ϕ_u orbitals is also detected in the β

https://doi.org/10.1021/jacsau.3c00838
JACS Au 2024, 4, 1134−1141

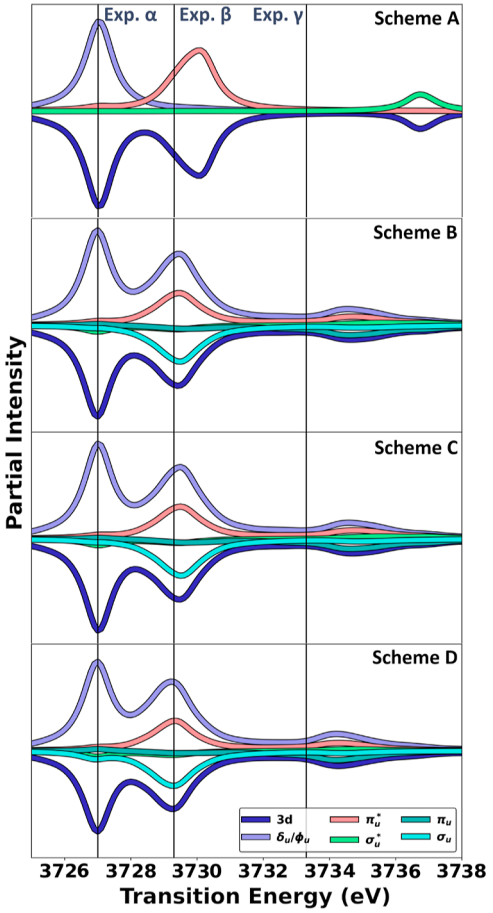

Figure 4. Partial intensity analysis of the uranyl M_4-edge spectrum. The normalized intensity of each excitation is projected onto the molecular orbital space (see the Methods section).

peak in addition to features originating from $3d_{3/2}$ to π_u^* transitions. This observation raises questions as the spectral characteristics would typically produce a single peak if the δ_u/ϕ_u orbitals were truly nonbonding and exhibited degenerate 5f character.

There are two possible mechanisms that can give rise to δ_u/ϕ_u orbital splitting in the M_4-edge HR-XANES spectrum. If δ_u/ϕ_u are mixed with σ_u and π_u, it will lead to a frontier orbital and spectral splitting. However, the orbital analysis does not show any mixing between these orbitals. The second possible mechanism will be that these peaks arise from the shake-up transitions, which involved two electron processes in the absorption spectrum.

To gain deeper insights into the nature of the observed transitions, we conducted an analysis of electron transitions between orbital pairs and corresponding intensities (see the Methods section), as shown in Figure 5. These figures provide a population analysis for each M_4-edge excitation, offering valuable information about the contributing orbitals. Detailed analyses of the CI vectors for M_4-edge states were carried out using Scheme D. The results, including percentages of single and double electron excitations in each state and their leading contributions, are presented in the Supporting Information.

For the α peak shown in Figure 5a, the excitations involve one-electron transitions from the $3d_{3/2}$ orbital to the nonbonding δ_u/ϕ_u orbitals, aligning with our initial expectations. Notably, a substantial proportion of excitations also stems from two electron excitations involving coupled transitions from the σ_u and $3d_{3/2}$ orbitals, manifesting clear shake-up characteristics. However, shake-up transitions in this specific region exhibit a small transition dipole moment. As a result, a total of 91% of the intensity in the region of the α peak can be attributed to the one-electron $3d_{3/2} \rightarrow \delta_u/\phi_u$ transition, as shown in Figure 5d. This means that, despite a considerable presence of shake-up phenomena originating from the valence transitions between δ_u/ϕ_u orbitals, these remain spectroscopically dark within the α peak spectral range.

In contrast, the β peak displayed in Figure 5b exhibits more complex behavior with contributions from multiple two-electron excitations. This peak involves many simultaneous transitions from both the $3d_{3/2}$ and σ_u orbitals to the δ_u/ϕ_u nonbonding orbitals, as well as the π_u^* antibonding orbitals. Such observations again indicate the presence of shake-up transitions, representing concerted processes involving core-electron and valence-electron excitations. However, as shown in Figure 5e, the majority of the transitions have a small contribution to the dipole oscillator strength, which is limited by symmetry considerations. Approximately 60% of the intensity in the region of the β peak can be ascribed to transitions between the $3d_{3/2}$ and δ_u/ϕ_u orbitals. The remaining roughly 40% of the intensity comes from contributions from the σ_u to π_u^* transitions, signifying a pronounced shake-up feature.

Analyzing the γ peak depicted in Figure 5c reveals an even more pronounced shake-up feature. This peak involves excitations not only from the $3d_{3/2}$ core orbital but also from the π_u bonding orbitals to the δ_u/ϕ_u nonbonding orbitals and the π_u^* antibonding orbitals. Additionally, a transition into the experimentally assigned σ_u^* antibonding orbital is observed, although this spectral feature may be obscured by the presence of the shake-up peaks. Figure 5f shows that, similar to the β peak, only a small fraction of the shake-up transitions contributes to the dipole oscillator strength. In the region of the γ peak, 62% of the total intensity can be attributed to the $3d_{3/2}$ and δ_u/ϕ_u orbitals, with an additional 32% arising from π_u and π_u^*. The remaining 6% of the intensity involves the σ_u and σ_u^* orbitals.

CONCLUSIONS

In summary, we utilized variational relativistic MRCI methods to compute and analyze the X-ray M-edge absorption spectrum of uranyl. The obtained results demonstrate an excellent agreement between the computed and experimentally observed peak positions and intensities, emphasizing the significance of incorporating correlations from 5f and 6d bonding and antibonding orbitals. Including 5f and 6d orbital correlations reduces the percent errors in peak separations by an average of ~40%. This highlights the critical role these orbitals play in accurately describing the spectral characteristics.

Upon closer examination, it is clear that the experimentally determined spectral characteristics do not adequately account for key shake-up features. An estimated 33% of all electrons excited in the M_4-edge spectrum come from the valence 5f bonding orbitals, making a significant contribution to these shake-up phenomena. The presence of strong shake-up peaks within the uranyl M_4-edge spectral range has the potential to obscure the analysis of covalency in actinide complexes. These shake-up peaks represent concerted excitations involving core and valence electrons, contributing to a more comprehensive

https://doi.org/10.1021/jacsau.3c00838
JACS Au 2024, 4, 1134−1141

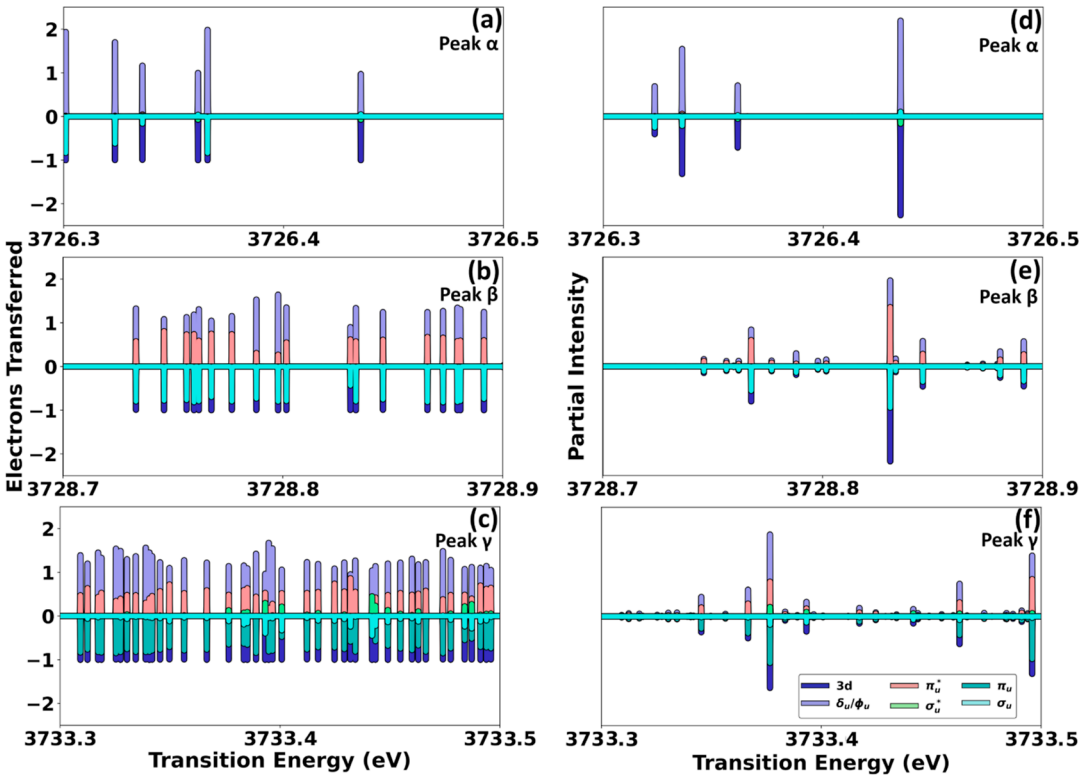

Figure 5. Transition population analysis for each M_4-edge excitation based on the calculation using Scheme D. Electron excitations from/to 6d orbitals are negligible and thus are not shown. The negative/positive values indicate the molecular orbitals from/to which the electrons are excited, respectively. (a–c) The electron populations in each calculated transition are for peaks α, β, and γ, respectively. (d–f) The partial normalized intensity for each calculated transition is shown in peaks α, β, and γ, respectively. Different colors represent various orbitals involved in the transitions, as illustrated in panel (f).

understanding of the electronic interactions and bonding nature.

METHODS

In this work, we use the relativistic Hamiltonian in the form of the X2C method,[23,25,34−50] which is similar to the normalized elimination of the small component (NESC) technique,[51−58] both allowing for variational treatment of relativistic corrections in electronic structure theory. The X2C and NESC approaches transform four-component Dirac–Hartree–Fock into an electron-only two-component method, where scalar relativistic and spin–orbit effects can be variationally included at the orbital level. We use an X2C state-averaged restricted active space self-consistent field (X2C-SA-RASSCF) method in the Kramers' unrestricted framework to generate the reference orbitals,[20,22,23,25] followed by an X2C-MRCI treatment of the dynamical correlation. The X2C-MRCI step is mapped onto the restricted active space (RAS) partitioning scheme,[22,59,60] which allows a natural extension to study X-ray spectra.[19,61−69] For details on the X2C-MRCI theory and implementation, we refer readers to ref 22.

The relativistic X2C-MRCI framework for the uranyl M_4-edge calculation starts with the 3d core-hole orbital optimization using X2C-RASSCF. A state-averaged X2C-RASSCF calculation is run with the four $3d_{3/2}$ orbitals in RAS1, the eight δ/ϕ orbitals in RAS2, and an empty RAS3. One electron is allowed to excite out of RAS1 and into RAS2, producing 32 core-electron excited states. All orbitals are optimized with respect to all 32 core-electron excited states to account for the core-hole relaxation. These orbitals are better suited for modeling the core-hole excited states necessary for subsequent spectrum generation.

In the following correlated X2C-MRCI treatment, three RASs are structured:

- RAS1: *Correlated core space* consists of spinor orbitals that are occupied in all reference determinants but can be excited in MRCI.
- RAS2/CASSCF: *Complete active space* consists of active spinor orbitals in the X2C-CASSCF reference.
- RAS3: *Correlated virtual space* consists of orbitals that are unoccupied in all reference determinants but can be occupied in MRCI.

After assigning orbitals in the three spaces, the X2C-MRCI excitation list can be generated given the correlation level of choice (e.g., single, double, or triple excitation). In this work, single-and double-electron excitations out of the RAS1 space are allowed. Introducing the RAS framework into the X2C-MRCI partitioning scheme gives rise to flexibility in both the choice of correlation space and excitation level and allows for an efficient generation and tracking of unique excited configurations, such as those in M-edge XAS. Since inner valence bonding orbitals are included in RAS1, the X2C-MRCI calculations will produce additional low-lying excited states. The energy-specific Davidson algorithm[70−72] is used to solve for only spectral features in the M-edge range.

For excitation from state I to state J, we evaluate $\delta\rho_p = \gamma_{pp}^{J} - \gamma_{pp}^{I}$. Here, γ_{pp} is the diagonal element of the one-particle reduced density matrix, corresponding to the p-th orbital occupation. $\delta\rho_p$ represents the change in orbital occupation upon the excitation. The negative and positive values of $\delta\rho_p$ indicate the MOs from and to which the electrons are excited, respectively. The partial oscillator strength can be computed as $f_p^{IJ} = \delta\rho_p f^{IJ}$, where f^{IJ} is the total oscillator strength for the excitation.

The molecular geometry for uranyl is linear with the U–O bond length set to be 1.760 Å taken from literature values.[73] The ANO-RCC-VTZP basis set[74−76] was applied to the uranium atom, and the aug-cc-pVTZ basis set[77] was utilized for the oxygen atoms. All calculations were performed in a development version of the Gaussian

https://doi.org/10.1021/jacsau.3c00838
JACS Au 2024, 4, 1134−1141

quantum chemistry package.[78] Neither point group symmetry nor Kramers symmetry was enforced in any of the calculations.

The experimental spectrum was measured for UO_2^{2+} in aqueous 1 M perchloric acid ($HClO_4$). Different chemical environments can result in a small variation of ±0.2 eV in the measured spectrum, manifested as a shift in the overall spectrum while leaving the peak splittings unchanged.[10] Since perchloride anion is a noncoordinating ligand and the environment-induced difference in spectral shift is not significant for the peak splittings, the computed results represent a generalized average of M_4 X-ray spectrum of UO_2^{2+}.

■ ASSOCIATED CONTENT

Supporting Information

The Supporting Information is available free of charge at https://pubs.acs.org/doi/10.1021/jacsau.3c00838.

Detailed analyses, including excitation energies, percentages of single- and double-electron excitations in each state, and their leading contributions (PDF)

■ AUTHOR INFORMATION

Corresponding Authors

Ping Yang − *Theoretical Division, Los Alamos National Laboratory, Los Alamos, New Mexico 87545, United States;* orcid.org/0000-0003-4726-2860; Email: pyang@lanl.gov

Xiaosong Li − *Department of Chemistry, University of Washington, Seattle, Washington 98195, United States;* orcid.org/0000-0001-7341-6240; Email: xsli@uw.edu

Authors

Jordan N. Ehrman − *Department of Chemistry, University of Washington, Seattle, Washington 98195, United States*

Kirill Shumilov − *Department of Chemistry, University of Washington, Seattle, Washington 98195, United States*

Andrew J. Jenkins − *Department of Chemistry, University of Washington, Seattle, Washington 98195, United States;* orcid.org/0000-0002-1014-5225

Joseph M. Kasper − *Theoretical Division, Los Alamos National Laboratory, Los Alamos, New Mexico 87545, United States;* orcid.org/0000-0002-3840-484X

Tonya Vitova − *Institute for Nuclear Waste Disposal (INE), Karlsruhe Institute of Technology, Karlsruhe D-76021, Germany;* orcid.org/0000-0002-3117-7701

Enrique R. Batista − *Theoretical Division, Los Alamos National Laboratory, Los Alamos, New Mexico 87545, United States;* orcid.org/0000-0002-3074-4022

Complete contact information is available at: https://pubs.acs.org/10.1021/jacsau.3c00838

Author Contributions

‖J.N.E., K.S., and A.J.J. contributed equally.

Notes

The authors declare no competing financial interest.

■ ACKNOWLEDGMENTS

The study of heavy-element complex is supported by the U.S. Department of Energy, Office of Science, Basic Energy Sciences, in the Heavy-Element Chemistry program (grant no. DE-SC0021100 to X.L. and contract DE-AC52-06NA25396 at Los Alamos National Laboratory). Computations were facilitated through the use of advanced computational, storage, and networking infrastructure provided by the Hyak supercomputer system at the University of Washington, funded by the Student Technology Fee. J.M.K. acknowledges funding from a Director's Postdoctoral Fellowship from Los Alamos National Laboratory (LANL). Los Alamos National Laboratory is operated by Triad National Security, LLC, for the National Nuclear Security Administration of U.S. DOE (contract 89233218CNA000001). J.N.E. acknowledges the Summer Graduate Research Associate Fellowship sponsored by the G. T. Seaborg Institute at LANL. T.V. acknowledges the funding from the European Research Council (ERC) Consolidator grant 2020 under the European Union's Horizon 2020 research and innovation programme (grant agreement no. 101003292, "The Actinide Bond").

■ REFERENCES

(1) Kaltsoyannis, N. Does Covalency Increase or Decrease Across the Actinide Series? Implications for Minor Actinide Partitioning. *Inorg. Chem.* **2013**, *52*, 3407−3413.

(2) Dam, H. H.; Reinhoudt, D. N.; Verboom, W. Multicoordinate Ligands for Actinide/Lanthanide Separations. *Chem. Soc. Rev.* **2007**, *36*, 367−377.

(3) Arnold, P. L.; McMullon, M. W.; Rieb, J.; Kühn, F. E. C−H Bond Activation by f-Block Complexes. *Angew. Chem., Int. Ed.* **2015**, *54*, 82−100.

(4) Batrice, R. J.; Eisen, M. S. Catalytic Insertion of E−H bonds (E= C, N, P, S) into Heterocumulenes by Amido−Actinide Complexes. *Chem. Sci.* **2016**, *7*, 939−944.

(5) Vallejo, K. D.; Kabir, F.; Poudel, N.; Marianetti, C. A.; Hurley, D. H.; Simmonds, P. J.; Dennett, C. A.; Gofryk, K. Advances in Actinide Thin Films: Synthesis, Properties, and Future Directions. *Rep. Prog. Phys.* **2022**, *85*, 123101.

(6) Pallares, R. M.; Abergel, R. J. Transforming Lanthanide and Actinide Chemistry with Nanoparticles. *Nanoscale* **2020**, *12*, 1339−1348.

(7) Bonato, L.; Virot, M.; Dumas, T.; Mesbah, A.; Dalodière, E.; Dieste Blanco, O.; Wiss, T.; Le Goff, X.; Odorico, M.; Prieur, D.; et al. Probing the local structure of nanoscale actinide oxides: a comparison between PuO_2 and ThO_2 nanoparticles rules out PuO_{2+x} hypothesis. *Nanoscale Adv.* **2020**, *2*, 214−224.

(8) Pepper, M.; Bursten, B. E. The electronic structure of actinide-containing molecules: a challenge to applied quantum chemistry. *Chem. Rev.* **1991**, *91*, 719−741.

(9) Neidig, M. L.; Clark, D. L.; Martin, R. L. Covalency in f-Element Complexes. *Coord. Chem. Rev.* **2013**, *257*, 394−406.

(10) Vitova, T.; Pidchenko, I.; Fellhauer, D.; Bagus, P. S.; Joly, Y.; Pruessmann, T.; Bahl, S.; Gonzalez-Robles, E.; Rothe, J.; Altmaier, M.; Denecke, M. A.; Geckeis, H. The Role of the 5f Valence Orbitals of Early Actinides in Chemical Bonding. *Nat. Commun.* **2017**, *8*, 16053.

(11) Sergentu, D.-C.; Duignan, T. J.; Autschbach, J. Ab Initio Study of Covalency in the Ground versus Core-Excited States and X-ray Absorption Spectra of Actinide Complexes. *J. Phys. Chem. Lett.* **2018**, *9*, 5583−5591.

(12) Bagus, P. S.; Schacherl, B.; Vitova, T. Computational and Spectroscopic Tools for the Detection of Bond Covalency in Pu(IV) Materials. *Inorg. Chem.* **2021**, *60*, 16090−16102.

(13) Cross, J. N.; Su, J.; Batista, E. R.; Cary, S. K.; Evans, W. J.; Kozimor, S. A.; Mocko, V.; Scott, B. L.; Stein, B. W.; Windorff, C. J.; Yang, P. Covalency in Americium(III) Hexachloride. *J. Am. Chem. Soc.* **2017**, *139*, 8667−8677.

(14) Löble, M. W.; Keith, J. M.; Altman, A. B.; Stieber, S. C. E.; Batista, E. R.; Boland, K. S.; Conradson, S. D.; Clark, D. L.; Lezama Pacheco, J.; Kozimor, S. A.; Martin, R. L.; Minasian, S. G.; Olson, A. C.; Scott, B. L.; Shuh, D. K.; Tyliszczak, T.; Wilkerson, M. P.; Zehnder, R. A. Covalency in Lanthanides. An X-ray Absorption Spectroscopy and Density Functional Theory Study of $LnCl_6^{x-}(x = 3, 2)$. *J. Am. Chem. Soc.* **2015**, *137*, 2506−2523.

(15) Minasian, S. G.; Keith, J. M.; Batista, E. R.; Boland, K. S.; Bradley, J. A.; Daly, S. R.; Kozimor, S. A.; Lukens, W. W.; Martin, R. L.; Nordlund, D.; Seidler, G. T.; Shuh, D. K.; Sokaras, D.; Tyliszczak, T.; Wagner, G. L.; Weng, T.-C.; Yang, P. Covalency in Metal − Oxygen Multiple Bonds Evaluated Using Oxygen K-edge Spectroscopy and Electronic Structure Theory. *J. Am. Chem. Soc.* **2013**, *135*, 1864−1871.
(16) Polly, R.; Schacherl, B.; Rothe, J.; Vitova, T. Relativistic Multiconfigurational *Ab Initio* Calculation of Uranyl 3d4f Resonant Inelastic X-ray Scattering. *Inorg. Chem.* **2021**, *60*, 18764−18776.
(17) Su, J.; Batista, E. R.; Boland, K. S.; Bone, S. E.; Bradley, J. A.; Cary, S. K.; Clark, D. L.; Conradson, S. D.; Ditter, A. S.; Kaltsoyannis, N.; Keith, J. M.; Kerridge, A.; Kozimor, S. A.; Löble, M. W.; Martin, R. L.; Minasian, S. G.; Mocko, V.; La Pierre, H. S.; Seidler, G. T.; Shuh, D. K.; Wilkerson, M. P.; Wolfsberg, L. E.; Yang, P. Energy-Degeneracy-Driven Covalency in Actinide Bonding. *J. Am. Chem. Soc.* **2018**, *140*, 17977−17984.
(18) Kasper, J. M.; Stetina, T. F.; Jenkins, A. J.; Li, X. Ab Initio Methods for L-edge X-ray Absorption Spectroscopy. *Chem. Phys. Rev.* **2020**, *1*, 011304.
(19) Jenkins, A. J.; Hu, H.; Lu, L.; Frisch, M. J.; Li, X. Two-Component Multireference Restricted Active Space Configuration Interaction for the Computation of L-Edge X-ray Absorption Spectra. *J. Chem. Theory Comput.* **2022**, *18*, 141−150.
(20) Jenkins, A. J.; Liu, H.; Kasper, J. M.; Frisch, M. J.; Li, X. Variational Relativistic Two-Component Complete-Active-Space Self-Consistent Field Method. *J. Chem. Theory Comput.* **2019**, *15*, 2974−2982.
(21) Knecht, S.; Jensen, H.; Saue, T. Relativistic quantum chemical calculations show that the uranium molecule U2 has a quadruple bond. *Nat. Chem.* **2019**, *11*, 40−44.
(22) Hu, H.; Jenkins, A. J.; Liu, H.; Kasper, J. M.; Frisch, M. J.; Li, X. Relativistic Two-Component Multireference Configuration Interaction Method with Tunable Correlation Space. *J. Chem. Theory Comput.* **2020**, *16*, 2975−2984.
(23) Lu, L.; Hu, H.; Jenkins, A. J.; Li, X. Exact-Two-Component Relativistic Multireference Second-Order Perturbation Theory. *J. Chem. Theory Comput.* **2022**, *18*, 2983−2992.
(24) Hoyer, C. E.; Lu, L.; Hu, H.; Shumilov, K. D.; Sun, S.; Knecht, S.; Li, X. Correlated Dirac−Coulomb−Breit Multiconfigurational Self-Consistent-Field Methods. *J. Chem. Phys.* **2023**, *158*, 044101.
(25) Hoyer, C. E.; Hu, H.; Lu, L.; Knecht, S.; Li, X. Relativistic Kramers-Unrestricted Exact-Two-Component Density Matrix Renormalization Group. *J. Phys. Chem. A* **2022**, *126*, 5011−5020.
(26) Costa Peluzo, B. M. T.; Kraka, E. Uranium: The Nuclear Fuel Cycle and Beyond. *Int. J. Mol. Sci.* **2022**, *23*, 4655.
(27) Wadt, W. R. Why UO $_2^{2+}$Is Linear and Isoelectronic ThO_2 Is Bent. *J. Am. Chem. Soc.* **1981**, *103*, 6053−6057.
(28) Kaltsoyannis, N. Computational Study of Analogues of the Uranyl Ion Containing the -N = U=N- Unit: Density Functional Theory Calculations on UO $_2^{2+}$, UON^+, UN_2, $UO(NPH_3)^{3+}$, $U(NPH_3)_2^{4+}$, $[UCl_4\{NPR_3\}_2]$(R = H, Me), and $[UOCl_4\{NP(C_6H_5)_3\}]^-$. *Inorg. Chem.* **2000**, *39*, 6009−6017.
(29) Denning, R. G.; Green, J. C.; Hutchings, T. E.; Dallera, C.; Tagliaferri, A.; Giarda, K.; Brookes, N. B.; Braicovich, L. Covalency in the Uranyl Ion: A Polarized x-Ray Spectroscopic Study. *J. Chem. Phys.* **2002**, *117*, 8008−8020.
(30) Wiebke, J.; Weigand, A.; Weissmann, D.; Glorius, M.; Moll, H.; Bernhard, G.; Dolg, M. Combined Computational and Experimental Study of Uranyl(VI) 1:2 Complexation by Aromatic Acids. *Inorg. Chem.* **2010**, *49*, 6428−6435.
(31) Misael, W. A.; Severo Pereira Gomes, A. Core Excitations of Uranyl in Cs2UO2Cl4 from Relativistic Embedded Damped Response Time-Dependent Density Functional Theory Calculations. *Inorg. Chem.* **2023**, *62*, 11589−11601.
(32) Stanistreet-Welsh, K.; Kerridge, A. Bounding $[AnO_2]^{2+}$ (An = U, Np) Covalency by Simulated O K-edge and An M-edge X-ray Absorption near-Edge Spectroscopy. *Phys. Chem. Chem. Phys.* **2023**, *25*, 23753−23760.
(33) Vitova, T.; Green, J. C.; Denning, R. G.; Löble, M.; Kvashnina, K.; Kas, J. J.; Jorissen, K.; Rehr, J. J.; Malcherek, T.; Denecke, M. A. Polarization Dependent High Energy Resolution X-ray Absorption Study of Dicesium Uranyl Tetrachloride. *Inorg. Chem.* **2015**, *54*, 174−182.
(34) Dyall, K. G. Interfacing Relativistic and Nonrelativistic Methods. I. Normalized Elimination of the Small Component in the Modified Dirac Equation. *J. Chem. Phys.* **1997**, *106*, 9618−9626.
(35) Dyall, K. G. Interfacing Relativistic and Nonrelativistic Methods. II. Investigation of a Low-Order Approximation. *J. Chem. Phys.* **1998**, *109*, 4201−4208.
(36) Kutzelnigg, W.; Liu, W. Quasirelativistic Theory Equivalent to Fully Relativistic Theory. *J. Chem. Phys.* **2005**, *123*, 241102.
(37) Liu, W.; Peng, D. Infinite-Order Quasirelativistic Density Functional Method Based on the Exact Matrix Quasirelativistic Theory. *J. Chem. Phys.* **2006**, *125*, 044102.
(38) Peng, D.; Liu, W.; Xiao, Y.; Cheng, L. Making Four- and Two-Component Relativistic Density Functional Methods Fully Equivalent Based on the Idea of from Atoms to Molecule. *J. Chem. Phys.* **2007**, *127*, 104106.
(39) Iliaš, M.; Saue, T. An infinite-order two-component relativistic Hamiltonian by a simple one-step transformation. *J. Chem. Phys.* **2007**, *126*, 064102.
(40) Liu, W.; Peng, D. Exact Two-component Hamiltonians Revisited. *J. Chem. Phys.* **2009**, *131*, 031104.
(41) Liu, W. Ideas of Relativistic Quantum Chemistry. *Mol. Phys.* **2010**, *108*, 1679−1706.
(42) Saue, T. Relativistic Hamiltonians for Chemistry: A Primer. *ChemPhysChem* **2011**, *12*, 3077−3094.
(43) Li, Z.; Xiao, Y.; Liu, W. On the Spin Separation of Algebraic Two-Component Relativistic Hamiltonians. *J. Chem. Phys.* **2012**, *137*, 154114.
(44) Peng, D.; Middendorf, N.; Weigend, F.; Reiher, M. An Efficient Implementation of Two-Component Relativistic Exact-Decoupling Methods for Large Molecules. *J. Chem. Phys.* **2013**, *138*, 184105.
(45) Egidi, F.; Goings, J. J.; Frisch, M. J.; Li, X. Direct Atomic-Orbital-Based Relativistic Two-Component Linear Response Method for Calculating Excited-State Fine Structures. *J. Chem. Theory Comput.* **2016**, *12*, 3711−3718.
(46) Goings, J. J.; Kasper, J. M.; Egidi, F.; Sun, S.; Li, X. Real Time Propagation of the Exact Two Component Time-Dependent Density Functional Theory. *J. Chem. Phys.* **2016**, *145*, 104107.
(47) Konecny, L.; Kadek, M.; Komorovsky, S.; Malkina, O. L.; Ruud, K.; Repisky, M. Acceleration of Relativistic Electron Dynamics by Means of X2C Transformation: Application to the Calculation of Nonlinear Optical Properties. *J. Chem. Theory Comput.* **2016**, *12*, 5823−5833.
(48) Egidi, F.; Sun, S.; Goings, J. J.; Scalmani, G.; Frisch, M. J.; Li, X. Two-Component Non-Collinear Time-Dependent Spin Density Functional Theory for Excited State Calculations. *J. Chem. Theory Comput.* **2017**, *13*, 2591−2603.
(49) Liu, J.; Cheng, L. Relativistic Coupled-Cluster and Equation-of-Motion Coupled-Cluster Methods. *Wiley Interdiscip. Rev.: Comput. Mol. Sci.* **2021**, *11*, 1536.
(50) Sharma, P.; Jenkins, A. J.; Scalmani, G.; Frisch, M. J.; Truhlar, D. G.; Gagliardi, L.; Li, X. Exact-Two-Component Multiconfiguration Pair-Density Functional Theory. *J. Chem. Theory Comput.* **2022**, *18*, 2947−2954.
(51) Filatov, M.; Cremer, D. A New Quasi-Relativistic Approach for Density Functional Theory Based on the Normalized Elimination of the Small Component. *Chem. Phys. Lett.* **2002**, *351*, 259−266.
(52) Zou, W.; Filatov, M.; Cremer, D. Development and Application of the Analytical Energy Gradient for the Normalized Elimination of the Small Component Method. *J. Chem. Phys.* **2011**, *134*, 244117.
(53) Zou, W.; Filatov, M.; Cremer, D. Development, Implementation, and Application of an Analytic Second Derivative Formalism for the Normalized Elimination of the Small Component Method. *J. Chem. Theory Comput.* **2012**, *8*, 2617−2629.

https://doi.org/10.1021/jacsau.3c00838
JACS Au 2024, 4, 1134−1141

(54) Filatov, M.; Zou, W.; Cremer, D. Relativistically Corrected Electric Field Gradients Calculated with the Normalized Elimination of the Small Component Formalism. *J. Chem. Phys.* **2012**, *137*, 054113.
(55) Zou, W.; Filatov, M.; Cremer, D. Analytical Energy Gradient for the Two-component Normalized Elimination of the Small Component Method. *J. Chem. Phys.* **2015**, *142*, 214106.
(56) Zou, W.; Guo, G.; Suo, B.; Liu, W. Analytic Energy Gradients and Hessians of Exact Two-Component Relativistic Methods: Efficient Implementation and Extensive Applications. *J. Chem. Theory Comput.* **2020**, *16*, 1541−1554.
(57) Makoś, M. Z.; Zou, W.; Freindorf, M.; Kraka, E. Metal−ring Interactions in Actinide Sandwich Compounds: A Combined Normalized Elimination of the Small Component and Local Vibrational Mode Study. *Mol. Phys.* **2020**, *118*, No. e1768314.
(58) Peluzo, B. M. T. C.; Makoś, M. Z.; Moura, R. T. J.; Freindorf, M.; Kraka, E. Linear versus Bent Uranium(II) Metallocenes: A Local Vibrational Mode Study. *Inorg. Chem.* **2023**, *62*, 12510−12524.
(59) Olsen, J.; Roos, B. O.; Jo/rgensen, P.; Jensen, H. J. A. Determinant Based Configuration Interaction Algorithms for Complete and Restricted Configuration Interaction Spaces. *J. Chem. Phys.* **1988**, *89*, 2185−2192.
(60) Malmqvist, P. Å.; Rendell, A.; Roos, B. O. The Restricted Active Space Self-consistent-field Method, Implemented with a Split Graph Unitary Group Approach. *J. Phys. Chem.* **1990**, *94*, 5477−5482.
(61) Engel, N.; Bokarev, S. I.; Suljoti, E.; Garcia-Diez, R.; Lange, K. M.; Atak, K.; Golnak, R.; Kothe, A.; Dantz, M.; Kühn, O.; Aziz, E. F. Chemical Bonding in Aqueous Ferrocyanide: Experimental and Theoretical X-ray Spectroscopic Study. *J. Phys. Chem. B* **2014**, *118*, 1555−1563.
(62) Guo, M.; Sørensen, L. K.; Delcey, M. G.; Pinjari, R. V.; Lundberg, M. Simulations of Iron K Pre-edge X-ray Absorption Spectra Using the Restricted Active Space Method. *Phys. Chem. Chem. Phys.* **2016**, *18*, 3250−3259.
(63) Pinjari, R. V.; Delcey, M. G.; Guo, M.; Odelius, M.; Lundberg, M. Restricted Active Space Calculations of L-edge X-ray Absorption Spectra: From Molecular Orbitals to Multiplet States. *J. Chem. Phys.* **2014**, *141*, 124116.
(64) Pinjari, R. V.; Delcey, M. G.; Guo, M.; Odelius, M.; Lundberg, M. Cost and Sensitivity of Restricted Active-space Calculations of Metal L-edge X-ray Absorption Spectra. *J. Comput. Chem.* **2016**, *37*, 477−486.
(65) Delcey, M. G.; Sørensen, L. K.; Vacher, M.; Couto, R. C.; Lundberg, M. Efficient Calculations of a Large Number of Highly Excited States for Multiconfigurational Wavefunctions. *J. Comput. Chem.* **2019**, *40*, 1789−1799.
(66) Bokarev, S. I.; Dantz, M.; Suljoti, E.; Kühn, O.; Aziz, E. F. State-dependent electron delocalization dynamics at the solute-solvent interface: Soft-x-ray absorption spectroscopy and Ab initio calculations. *Phys. Rev. Lett.* **2013**, *111*, 083002.
(67) Lundberg, M.; Delcey, M. G. In *Transition Metals in Coordination Environments: Computational Chemistry and Catalysis Viewpoints*; Broclawik, E., Borowski, T., Radoń, M., Eds.; Springer International Publishing: Cham, 2019; pp 185−217.
(68) Josefsson, I.; Kunnus, K.; Schreck, S.; Föhlisch, A.; de Groot, F.; Wernet, P.; Odelius, M. Ab Initio Calculations of X-ray Spectra: Atomic Multiplet and Molecular Orbital Effects in a Multiconfigurational SCF Approach to the L-Edge Spectra of Transition Metal Complexes. *J. Phys. Chem. Lett.* **2012**, *3*, 3565−3570.
(69) Carreras, A.; Jiang, H.; Pokhilko, P.; Krylov, A. I.; Zimmerman, P. M.; Casanova, D. Calculation of Spin−orbit Couplings Using RASCI Spinless One-particle Density Matrices: Theory and Applications. *J. Chem. Phys.* **2020**, *153*, 214107.
(70) Liang, W.; Fischer, S. A.; Frisch, M. J.; Li, X. Energy-Specific Linear Response TDHF/TDDFT for Calculating High-Energy Excited States. *J. Chem. Theory Comput.* **2011**, *7*, 3540−3547.
(71) Peng, B.; Lestrange, P. J.; Goings, J. J.; Caricato, M.; Li, X. Energy-Specific Equation-of-Motion Coupled-Cluster Methods for High-Energy Excited States: Application to K-Edge X-Ray Absorption Spectroscopy. *J. Chem. Theory Comput.* **2015**, *11*, 4146−4153.
(72) Lestrange, P. J.; Nguyen, P. D.; Li, X. Calibration of Energy-Specific TDDFT for Modeling K-Edge XAS Spectra of Light Elements. *J. Chem. Theory Comput.* **2015**, *11*, 2994−2999.
(73) Allen, P.; Bucher, J.; Shuh, D.; Edelstein, N.; Reich, T. Investigation of Aquo and Chloro Complexes of UO_2^{2+}, NpO^{2+}, Np^{4+}, and Pu^{3+} by X-ray Absorption Fine Structure Spectroscopy. *Inorg. Chem.* **1997**, *36*, 4676−4683.
(74) Roos, B. O.; Lindh, R.; Malmqvist, P.-Å.; Veryazov, V.; Widmark, P.-O. Main Group Atoms and Dimers Studied with a New Relativistic ANO Basis Set. *J. Phys. Chem. A* **2004**, *108*, 2851−2858.
(75) Roos, B. O.; Lindh, R.; Malmqvist, P.-Å.; Veryazov, V.; Widmark, P.-O. New Relativistic ANO Basis Sets for Transition Metal Atoms. *J. Phys. Chem. A* **2005**, *109*, 6575−6579.
(76) Roos, B. O.; Lindh, R.; Malmqvist, P.-Å.; Veryazov, V.; Widmark, P.-O.; Borin, A. C. New Relativistic Atomic Natural Orbital Basis Sets for Lanthanide Atoms with Applications to the Ce Diatom and LuF_3. *J. Phys. Chem. A* **2008**, *112*, 11431−11435.
(77) Dunning, T. H. Gaussian Basis Sets for Use in Correlated Molecular Calculations. I. the Atoms Boron Through Neon and Hydrogen. *J. Chem. Phys.* **1989**, *90*, 1007−1023.
(78) Frisch, M. J.; Trucks, G. W.; Schlegel, H. B.; Scuseria, G. E.; Robb, M. A.; Cheeseman, J. R.; Scalmani, G.; Barone, V.; Petersson, G. A.; Nakatsuji, H.; Li, X.; Caricato, M.; Marenich, A. V.; Bloino, J.; Janesko, B. G.; Gomperts, R.; Mennucci, B.; Hratchian, H. P.; Ortiz, J. V.; Izmaylov, A. F.; Sonnenberg, J. L.; Williams-Young, D.; Ding, F.; Lipparini, F.; Egidi, F.; Goings, J.; Peng, B.; Petrone, A.; Henderson, T.; Ranasinghe, D.; Zakrzewski, V. G.; Gao, J.; Rega, N.; Zheng, G.; Liang, W.; Hada, M.; Ehara, M.; Toyota, K.; Fukuda, R.; Hasegawa, J.; Ishida, M.; Nakajima, T.; Honda, Y.; Kitao, O.; Nakai, H.; Vreven, T.; Throssell, K.; Montgomery, J. A.; Peralta, J. E.; Ogliaro, F.; Bearpark, M. J.; Heyd, J. J.; Brothers, E. N.; Kudin, K. N.; Staroverov, V. N.; Keith, T. A.; Kobayashi, R.; Normand, J.; Raghavachari, K.; Rendell, A. P.; Burant, J. C.; Iyengar, S. S.; Tomasi, J.; Cossi, M.; Millam, J. M.; Klene, M.; Adamo, C.; Cammi, R.; Ochterski, J. W.; Martin, R. L.; Morokuma, K.; Farkas, O.; Foresman, J. B.; Fox, D. J. *Gaussian Development Version Revision J.14+*; Gaussian Inc.: Wallingford CT, 2023.

https://doi.org/10.1021/jacsau.3c00838
JACS Au 2024, 4, 1134−1141